Structural Chemistry (2021) 32:1473–1488
https://doi.org/10.1007/s11224-020-01690-x

ORIGINAL RESEARCH

Electronic structures, bonding, and spin state energetics of biomimetic mononuclear and bridged dinuclear iron complexes: a computational examination

Monika[1] · Oval Yadav[1] · Hemlata Chauhan[1] · Azaj Ansari[1]

Received: 13 October 2020 / Accepted: 19 November 2020 / Published online: 15 January 2021
© Springer Science+Business Media, LLC, part of Springer Nature 2021

Abstract
Mononuclear and dinuclear iron complexes are found as key intermediates in many synthetic and biocatalytic reactions, since many of these species are transient and have high catalytic abilities. However, there is still demanding and challenging to theoretical study on structures, bonding, magnetic interactions and reactivity of iron species. Here, we have discussed a detailed computational study on Fe(III/IV/V)–O/O_2 and Fe(IV)–μ-O/O_2–Fe(IV) species using a dispersion-corrected (B3LYP-D2) density functional method. By computing all the possible spin states for these species, we have predicted the ground state and structure-function relationships in their ground states and analyzed the bonding aspects of these species on employing MO analysis. We have also discussed the shifting of iron centers out of the plane and magnetic coupling between iron and iron/oxygen centers. A computed significant spin density on the oxygen can be a witness for reactivity during the C–H and O–H bond activation. Our DFT studies are also in general agreement with the available experimental data.

Keywords Tetraamido macrocyclic ligand · Iron species · Density functional calculations · Electronic structures · Magnetic coupling

Introduction

Nonheme mononuclear and dinuclear complexes are involved in many catalytic reactions such as C–H activation, oxygen transfer, alcohol oxidation, and deformylation reactions [1–7]. C–H bond activation in hydrocarbons is highly inert, and biomimetic species can provide a direct way to introduce functional groups, cost-effectively, and has high industrial applications [8–10]. C–H bond activation is inspired by models of CytP450 and Rieske dioxygenase and these hydroxylate unactivated C–H bonds with higher selectivity at fast rates [11, 12]. Selective functionalization of the C–H bond in organic compounds is a "grand challenge" in catalysis science [13–18]. To carry out selective C–H bond activation, many heme [19–21] and nonheme [22–29] iron-containing complexes have been used with dioxygen as an oxidant. Dioxygen (O_2) is an ideal oxidant due to several reasons as it is abundant in nature, is a renewable chemical oxidant, has water as a byproduct, and is nontoxic at most of the conditions, and its reduction potential is more than sufficient to carry many chemical transformations [30–35]. Nonheme complexes with a tetradentate N-atom donor ligand having cis labile sites (FeN_4) show great promise for selective C–H bond activation [36–39]. Iron is ubiquitous, has low toxicity, and can exist in multiple redox states making its chemistry interesting and acts as a key intermediate in many biotransformation reactions, occurring via C–H and O–H activation, including biological O_2 activation [40–45].

A tetraamido macrocyclic ligand (TAML) activator is widely used in chemical and biological agents such as petroleum refining, water treatment, textiles, and cleaning [46]. TAML activators have about 10,000 turnovers per hour in many applications [47]. The TAML-coordinated metal species being environment friendly have been tested [48]. To investigate the catalytic properties, many experimental and theoretical studies such as Mossbauer, EPR, density functional theory (DFT), and transient- and steady-state kinetics have been used [39, 49, 50]. In the last two decades, the tetradentate TAML-ligated iron species becomes a popular oxidant to

✉ Azaj Ansari
ajaz.alam2@gmail.com

[1] Department of Chemistry, Central University of Haryana, Mahendergarh, Haryana 123031, India

achieve an effective small biomimetic molecule of oxidizing enzymes for green oxidation chemistry [30, 51]. It has biological elements like C, H, N, O, and Fe and is devoid of toxic functionalities [52]. There are several Fe–TAML complexes such as mononuclear iron oxo/peroxo/superoxo/hydroperoxo as well as oxygen-bridged dinuclear species that are observed in the previous literature [50, 53–56]. Some of the species are also well characterized by X-rays and spectroscopic parameters [49, 50, 57]. These species are also important intermediates generated during various metal-mediated catalytic transformation reactions such as alkane hydroxylation, olefin epoxidation, and sulfoxidation [58–74] occurring via C–H bond activation. These reactions are also important in synthetic pharmaceutical [13] and biological processes such as medicine, photosystem II, and naphthalene dioxygenase [75, 76].

The growing interest in TAML-ligated iron species motivated us to explore structures and spin-state energetics of mononuclear oxo/peroxo/superoxo/hydroperoxo and oxygen-bridged dinuclear species as a possible oxidant in many catalytical transformation reactions. Here, we would like to underpin and compare electronic structures, bonding, magnetic interactions, and spin-state energetic aspects of Fe(III/IV/V)–O/O_2 and Fe(IV)–μ-O_1/O_2–Fe(IV) species. By a study of structures and bonding of the species, we also like to comment on their reactivity.

Computational details

All calculations were carried out by using Gaussian09 programs [77]. In our earlier work, we have performed DFT calculations on iron species employing a bunch of functionals such as B3LYP, B3LYP-D2, wB97XD, B97D, M06-2X, OLYP, TPPSh, and MP2 methods [71, 73]. Among the tested functionals, B3LYP incorporating dispersion correction (B3LYP-D2 functional) was found to be superior in predicting the correct spin ground state of iron species [71, 73]. So here we have restricted geometry optimizations using only the B3LYP-D2 functional [78]. The LACVP basis set comprising the LanL2DZ–Los Alamos effective core potential for the iron [79–81] and a 6-31G [82] basis set for the other atoms (C, H, N, and O) have been employed for geometry optimization. The identification of the geometry that is located at the lowest point on the potential energy surface is made by frequency calculations which were performed on optimized geometry and confirmed by the absence of imaginary frequencies, and free-energy corrections were also found by frequency calculation. Single point energy calculations were made by using a TZVP [75, 83, 84] basis set on all atoms of the optimized geometries. For computing the solvation energies using acetonitrile as a solvent, the PCM solvation model was used. The quoted DFT energies are B3LYP-D2 solvation including free-energy corrections with the TZVP basis set at the temperature of 298.15 K. From the optimized geometries, structural parameters, vibrational wavenumbers, and other molecular properties like HOMO-LUMO and NBO were analyzed. The vibrational energy distribution analysis (VEDA) program was used to calculate the partial energy distribution (PED) [85], by using PED fundamental vibrational modes which were characterized. Theoretical and valuable information about intra- and intermolecular charge transfer (ICT) and conjugation and hyperconjugation of the molecular system [86, 87] is provided by natural bonding orbital (NBO) analysis. Using the Mulliken population analysis (MPA) method with the B3LYP-D2 functional, charges on the atoms of complexes were calculated. In the Gaussian09 fragment approach available which was employed to aid smooth convergence. In the diiron species, the magnetic exchange between both the iron centers is calculated by employing the following spin Hamiltonian:

$$\widehat{\boldsymbol{H}} = -\boldsymbol{J}\ \mathbf{S_1}.\mathbf{S_2}$$

Where J is the magnetic exchange coupling constant; positive J values show the ferromagnetic coupling while negative J values show the antiferromagnetic coupling. Noodleman's broken symmetry is used to compute the magnetic exchange coupling (J) constant [88, 89]. A common notation of $^{mult}A_{spin\ state}$ is used throughout where the mult, A, and spin state denote the total multiplicity, the species, and the possible spin states, respectively.

Results and discussion

Here, we will thoroughly discuss the electronic structures, bonding nature, and spin state energetics of biomimetic $[Fe^{III}(TAML)]^-$ (species I) and its possible mononuclear derivatives end-on $[(TAML)Fe^{IV}–\eta^1–O_2]^{\bullet-}$ (species II), side-on $[(TAML)Fe^{IV}–(\eta^2–O_2)]^{2-}$ (species IIIa), $[(TAML)Fe^{III}–(\eta^2–O_2)]^{3-}$ (species IIIb), $[(TAML)Fe^{IV}–OOH]^-$ (species IV), $[(TAML)Fe^{IV}–O]^{2-}$ species (V), and $[(TAML)Fe^{V}–O]^-$ species (VI) and dinuclear derivatives $[(TAML)Fe^{IV}–\mu O–(TAML)Fe^{IV}]^{2-}$ (species VII) and $[(TAML)Fe^{IV}–\mu O_2–Fe^{IV}(TAML)]^{2-}$ (species VIII) followed by a comparative study.

Electronic structure and energetics of $[Fe^{III}(TAML)]^-$ (species I)

It is a tetraamido macrocyclic species containing the iron ion, which is a very efficient and selective catalyst [22–29]. In species I (See Scheme 1), iron is surrounded by four deprotonated N-amido ligands and is almost square planar species [39]. This is well characterized by X-ray, UV-vis, EPR, and EXAFS [39]. We have optimized species I on the surfaces of $S = 5/2$ (sextet; $^6I_{hs}$) and $S = 3/2$ (quartet; $^4I_{is}$), and our DFT calculations reveal that the quartet state is computed

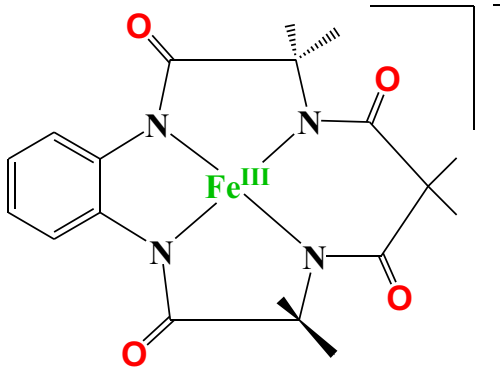

Scheme 1 A schematic diagram of tetraamido macrocyclic ligand-coordinated iron $[Fe^{III}(TAML)]^-$ species [39, 50]

to be the ground state and the sextet state lies at 89.0 kJ/mol higher in energy (see Fig. 1). This ground state is also supported by the experimental report [39]. The optimized structure of the ground state and the corresponding spin density plot are shown in Fig. 2a,b. The computed Fe–N_{avg} bond length of the ground state is found to be 1.865 Å, and this is in good agreement with the X-ray structure (see Table S1 of ESI) [39]. A spin density of $\rho = 2.663$ is located at the iron center (see Fig. 2b and Table S2 of ESI). The eigenvalue plot of the ground state is shown in Fig. S1 of ESI, and the electronic configuration at the metal center is found to be $(d_{yz})^2$, $(d_{xz})^1$, $(d_z^2)^1$, $(d_{xy})^1$, and $(d_{x^2-y^2})^0$. The HOMO-LUMO gap of the ground state is 4.446 eV (see Fig. 2c). By the reaction of $[Fe^{III}(TAML)]^-$ species with dioxygen, it can form mononuclear end-on $\{[(TAML)Fe^{IV}–\eta^1–O_2]^{\bullet-}\}$/side-on species $\{[(TAML)Fe^{III/IV}–\eta^2–O_2]^{3/2-}\}$ or dinuclear μ-oxo $\{[(TAMLFe^{IV})_2(\mu\text{-oxo})]^{2-}\}$/peroxo $\{[(TAMLFe^{IV})_2(\text{peroxo}(O_2)]^{2-}\}$bridged species which can also consequently form iron(IV/V)-oxo species [55]. After reactions of species I with dioxygen, the iron metal center is no longer in the plane but it gets out of the plane due to repulsion between charges of the coordinated nitrogen atoms and the axial ligands that forces the iron atom out of the plane. The distance of the shift of iron metal out of the plane depends upon the elastic force that drives the iron metal back into the plane [39].

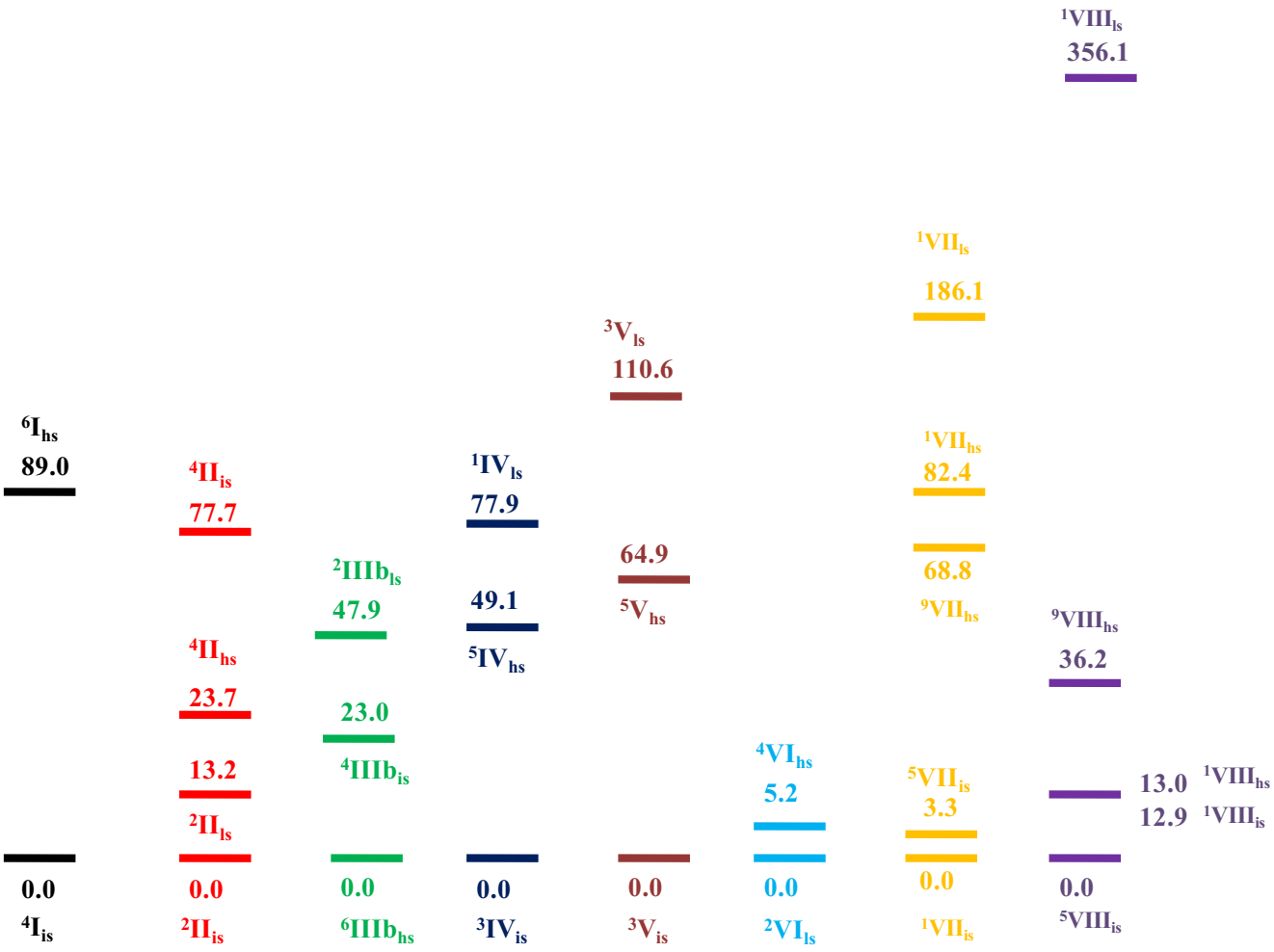

Fig. 1 B3LYP-D2-computed relative energies (in kJ/mol) of species I–VIII

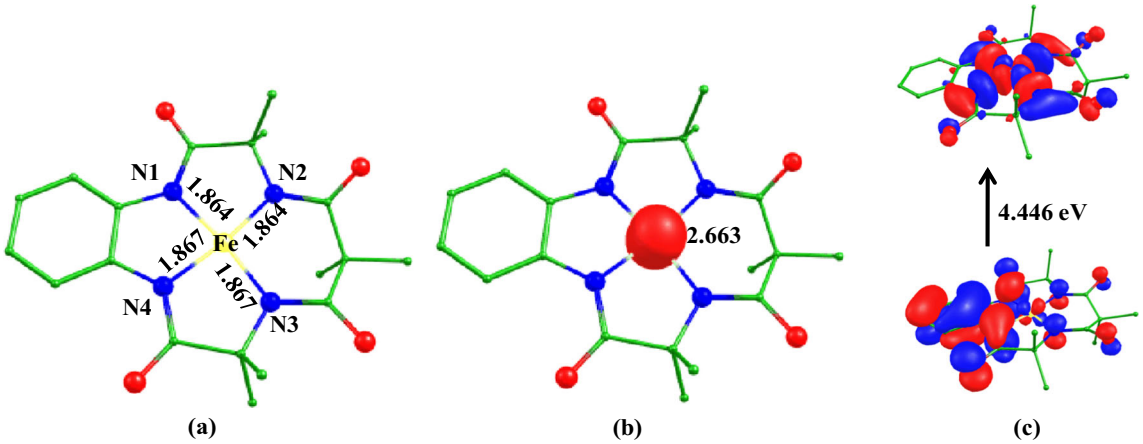

Fig. 2 **a** B3LYP-D2-optimized structure of $^4I_{is}$ (bond length in Å) and **b** its spin density plot and **c** HOMO-LUMO frontier molecular orbitals of $^4I_{is}$

Electronic structure and energetics of end-on [(TAML)Fe^{IV}–η^1–O_2]$^{\bullet-}$ (species II)

When the binding mode of oxygen is η^1, it can generate end-on iron superoxo species [90, 91]. Five spin interactions can be possible due to the presence of four unpaired electrons at the iron center and one unpaired electron at distal oxygen (see Scheme S1 of ESI). We have optimized all spin states of this species except $^6II_{hs}$ (due to the spin convergence issue). The antiferromagnetically coupled intermediate spin state ($^2II_{is}$) is found to be the ground state with the $^4II_{hs}$, $^4II_{is}$, and $^2II_{is}$ lying at 23.8, 77.7, and 13.2 kJ/mol, respectively (see Table S3 of ESI), and the ground state is also inconsistent with similar species in the previous report [56]. The optimized structure and spin density plot of the ground state are shown in Fig. 3a,b. The average Fe–N_{avg} bond of species II is larger than that of species I by 0.013 Å. The Fe–O_1 and O_1–O_2 bond lengths are computed to be 2.173 Å and 1.296 Å, respectively. The O_1–O_2 bond length is in agreement with the other metal superoxo species that are ca. 1.2–1.3 Å [91–96]. The stretching frequencies of the Fe–O and O–O bonds are computed to be ν314 cm^{-1} and ν1200 cm^{-1} that are also in agreement with the calculated stretching frequency of other superoxide species [91–95]. The iron center of this species is found to be shifted by 0.08 Å (see Table S4 of ESI) above the plane along with the axial bond concerning species I, and this is due to repulsion between charges of equatorial ligated nitrogen atoms and axial superoxo ligands that forces the iron atom out of the plane and suggested species II is relatively less planar. The HOMO-LUMO gap of species II is 1.524 eV (see Fig. 3c), and the gap is smaller than that of species I. The eigenvalue plot of the ground state is shown in Fig. 4, and the electronic configuration at the metal center is found to be $(d_{xz})^2$, $(d_{yz})^1$, $(d_{xy})^1$, $(d_{z^2})^0$, and $(d_{x^2-y^2})^0$. The spin density values at iron and distal oxygen centers are computed to be 2.586 and − 0.881 suggesting that the presence of antiferromagnetic coupling between them and a significant spin density at distal oxygen can activate the C–H and O–H bonds [56, 61, 96].

Electronic structure and energetics of side-on [(TAML)Fe^{IV}–(η^2–O_2)]$^{2-}$ (species IIIa) and [(TAML)Fe^{III}–(η^2–O_2)]$^{3-}$ (species IIIb)

When the binding mode of oxygen is η^2, the side-on species can be formed [95, 96]. Similar to species II, we have

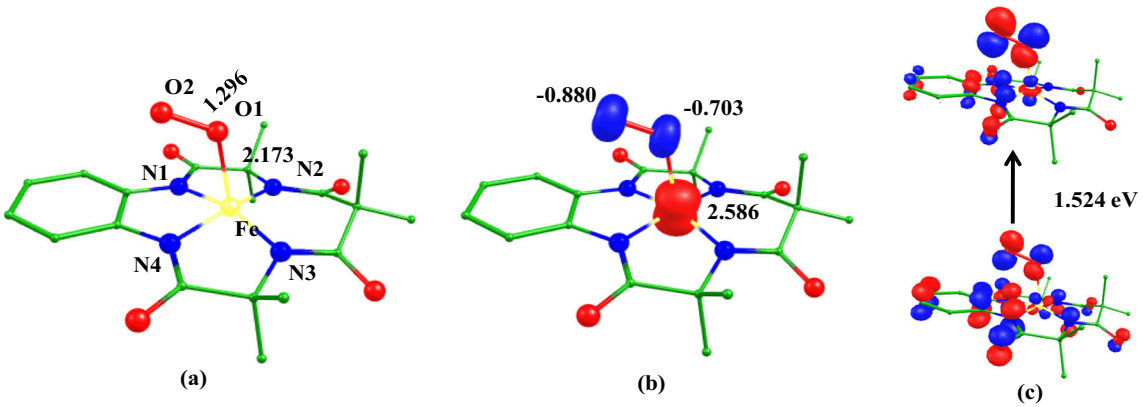

Fig. 3 **a** B3LYP-D2-optimized structure (bond length in Å) of $^2II_{is}$, **b** its spin density plot, and **c** the HOMO-LUMO frontier molecular orbitals of $^2II_{is}$

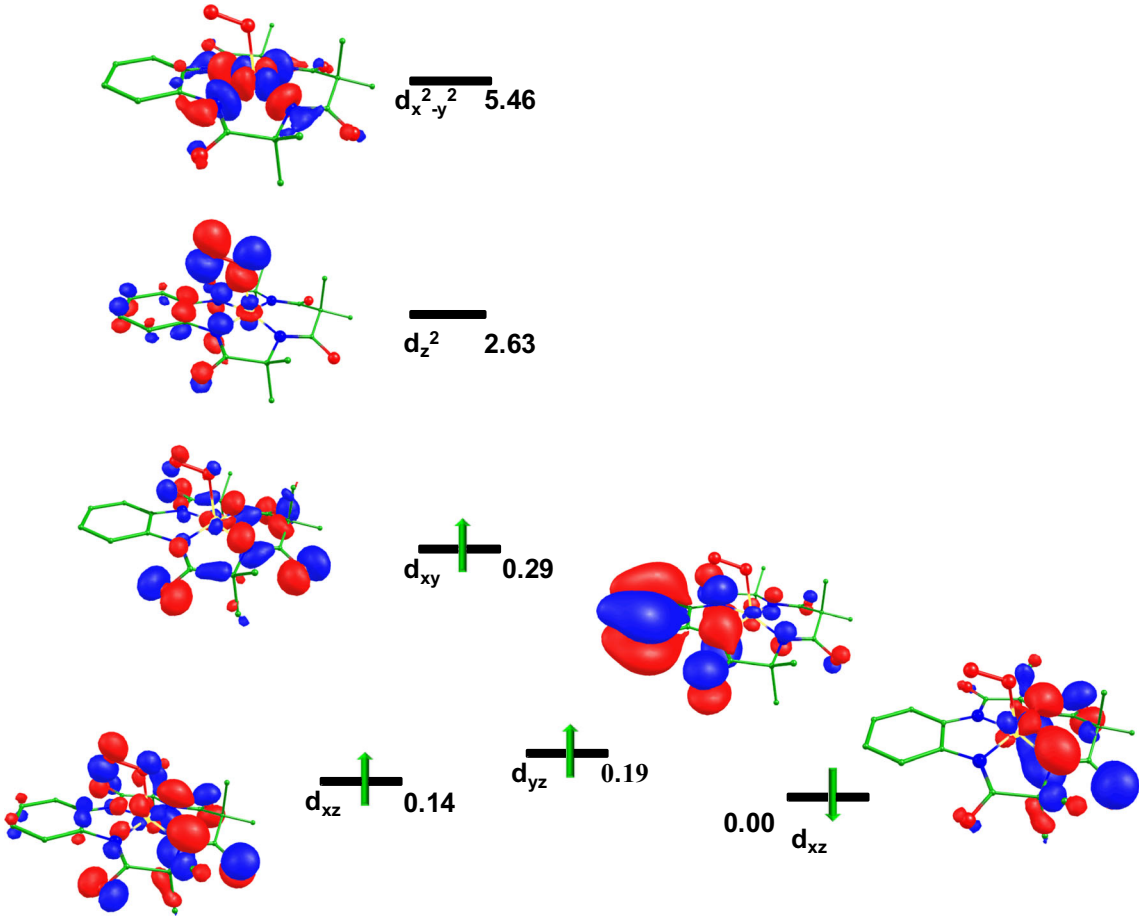

Fig. 4 Computed eigenvalue plot incorporating energies computed for *d*-based orbitals for alpha and beta spin corresponding to the ground state ($^2II_{is}$) (energies are given in eV)

tried to optimize all three possible spin surfaces (such as $^5IIIa_{hs}$, $^3IIIa_{is}$, and $^1IIIa_{ls}$) of species III but here we have got only one optimization, i.e., the low spin surface (see details in Fig. S2 of ESI). So, here we have also taken side-on species with oxidation state + 3 at the iron center and attempted to optimize all three possible spin states ($^6IIIb_{hs}$, $^4IIIb_{is}$, and $^2IIIb_{ls}$) for species IIIb. Our DFT calculations predicted that the sextet spin state ($^6IIIb_{hs}$) is found to be the ground state with $^4IIIb_{is}$ and $^2IIIb_{ls}$ lying at 23.0 kJ/mol and 47.9 kJ/mol, respectively. The optimized structure and spin density plot of the ground state are shown in Fig. 5a,b. The Fe–N_{avg} bond is computed to be 2.093 Å, and this is higher than that of species II. The computed Fe–O_1 and Fe–O_2 bond lengths are 2.009 Å and 1.994 Å, respectively, which are also observed in similar architecture [97]. The computed parameters suggest that the oxygen binds with iron symmetrically. The iron–oxygen bond length is found to be smaller while the O_1–O_2 bond length is slightly higher than the lengths of end-on species II, and these are also confirmed by the computed stretching frequency of Fe–O (ν448 cm^{-1}) and O–O (ν821 cm^{-1}) bonds [94]. The computed bond angle of O_1–Fe–O_2 is found to be 45.1° indicating the pseudo-square pyramidal geometry of species IIIb. The shift in the position of the iron atom is computed to be 0.72 Å (see Table S4 of ESI). The spin density value of 3.887 is located at the iron center, and both the oxygen atoms occupied similar spin density that indicates a symmetrical binding mode (see Fig. 5b). The eigenvalue plot of the ground state is shown in Fig. S4 of ESI. The electronic configuration on Fe metal is found to be $(d_{xy})^1$, $(d_{xz})^1$, $(d_{yz})^1$, $(d_{z^2})^1$, and $(d_{x^2-y^2})^1$. The HOMO-LUMO gap of species IIIb is calculated to be 3.698 eV (see Fig. 5c), and this is greater than that of species II which may indicate the possibility of lesser electron transfer compared to that in species II. The significant spin densities at both the oxygen atoms can participate in catalytic reactions [61–64]. The NBO plots of the ground state show that orbital contributions between both the oxygen atoms and iron center are involved in making the σ-bond confirming the presence of the σ-bond between both the oxygen atoms and iron center (see Fig. S5 of ESI).

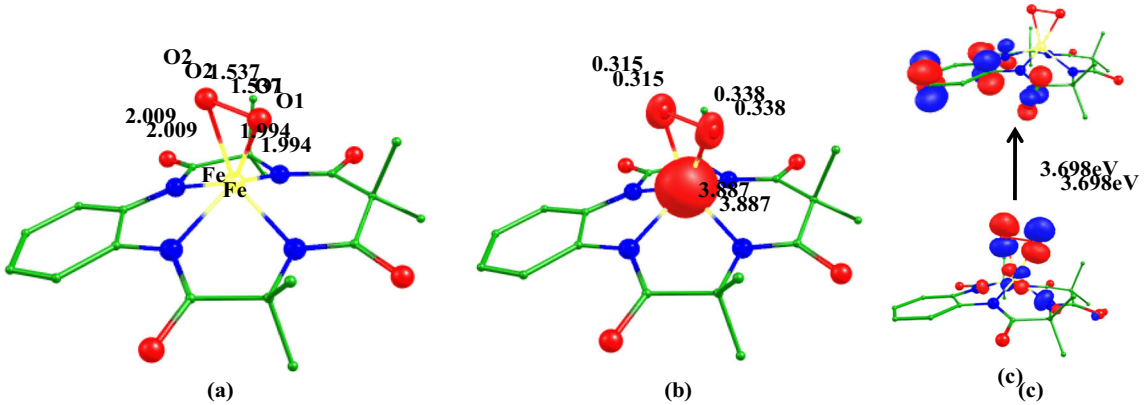

Fig. 5 **a** B3LYP-D2-optimized structure (bond length in Å) of ^{6}IIIb$_{hs}$, **b** its spin density plot, and **c** the HOMO-LUMO frontier molecular orbitals of ^{6}IIIb$_{hs}$

Electronic structure and energetics of hydroperoxo [(TAML)Fe^{IV}–OOH]$^{-}$ (species IV)

After the abstraction of hydrogen from organic substrates by superoxo/peroxo species, hydroperoxo species can be formed. Similar to the above species, there are three possible spin states of species IV, in which intermediate spin ($S = 1$) is found to be the ground state, and other spin states, $S = 2$ and $S = 0$, lie at 49.1 and 77.9 kJ/mol higher in energy, respectively. The optimized structure and spin density plot of the ground state are shown in Fig. 6. The Fe–O_1 and O_1–O_2 bond lengths are computed to be 1.889 Å and 1.486 Å, respectively. The Fe–O_1 bond length decreases while the O_1–O_2 bond length increases from superoxo species II. The computed shift in the position of the iron atom is computed to be 0.19 Å. The decrease in the Fe–O_1 bond length is due to the overlap between *d*-orbital of Fe and *p*-orbital of the oxygen atom. The HOMO-LUMO gap also decreases to 0.059 eV compared to that of species II and IIIb (see Fig. S6 of ESI). The NBO analysis shows that iron d_z^2 orbital has a 20.1% orbital contribution whereas p_z orbital of oxygen has a 79.9% orbital contribution (see the NBO plot in Fig. S7 of ESI). There is a reduction of spin density at the oxygen atoms. The eigenvalue plot is shown in Fig. 7. The electronic configuration at the metal center is found to be $(d_{xz})^2$, $(d_{yz})^1$, $(d_{xy,})^1$, $(d_z^2)^0$, and $(d_{x^2\text{-}y^2})^0$. The stretching frequency of the Fe–O and O–O bond is computed to be ν420 cm^{-1} and ν823 cm^{-1}, respectively, and a decrease in O–O stretching frequency by ν373 cm^{-1} compared to that of end-on [(TAML)Fe^{IV}-η^1-O_2]$^{\bullet-}$ species supported an increase in the O_1–O_2 bond length.

Electronic structure and spin energetics of [(TAML)Fe^{IV}–O]$^{2-}$ (species V)

The first direct evidence for the generation of a nonheme Fe^{IV}–O complex was reported by Grapperhaus et al. at the start of this millennium [98], and this is well characterized by X-ray and spectroscopy. Nonheme Fe^{IV}–O species became a popular active oxidant that can show reactivity towards C–H, O–H, N–H, oxygen atom transfer reactions, etc. in detail [68, 69]. Here, we have also optimized high (quintet, $S = 2$), intermediate (triplet, $S = 1$), and low spin (singlet, $S = 1$) states of the species, and our DFT calculations reveal that the triplet state is found to be the ground state with the quintet and singlet states lying at 86.4 kJ/mol and 112.6 kJ/mol higher in energy, respectively (see Fig. 1) and this ground state is inconsistent with earlier experimental and theoretical reports [54, 65–68]. The optimized structure and spin density plot of the ground state are shown in Fig. 8a,b. The calculated Fe–N_{avg} bond length is 1.929 Å, higher than that of species I (see Table S1

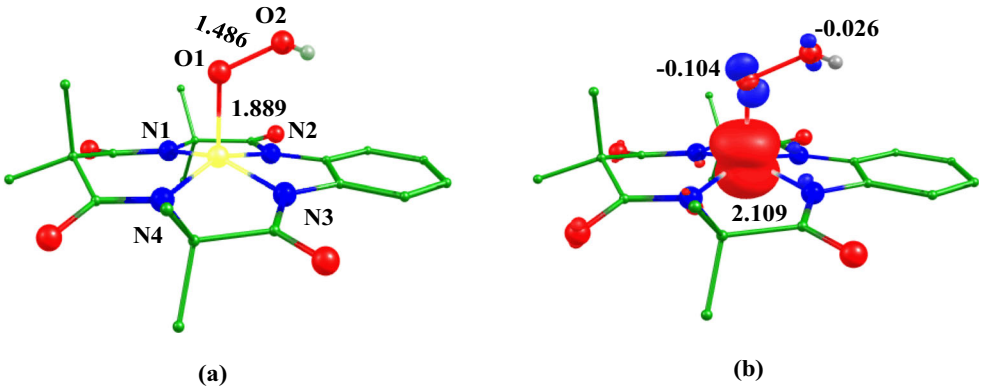

Fig. 6 **a** B3LYP-D2-optimized structure (bond length in Å) of ^{3}IV$_{is}$ and **b** its spin density plot

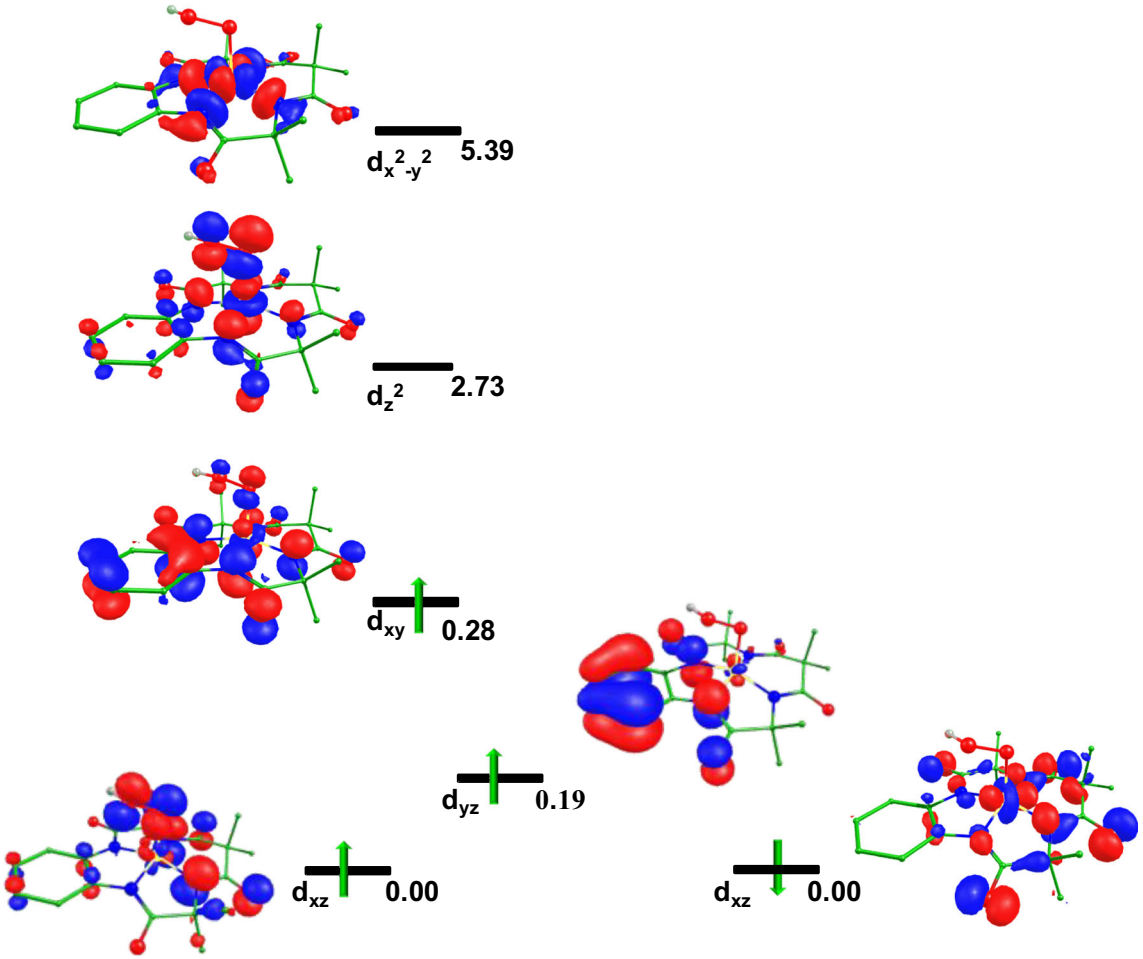

Fig. 7 Computed eigenvalue plot incorporating energies computed for *d*-based orbitals for alpha and beta spin corresponding to the ground state ($^3IV_{is}$) (energies are given in eV)

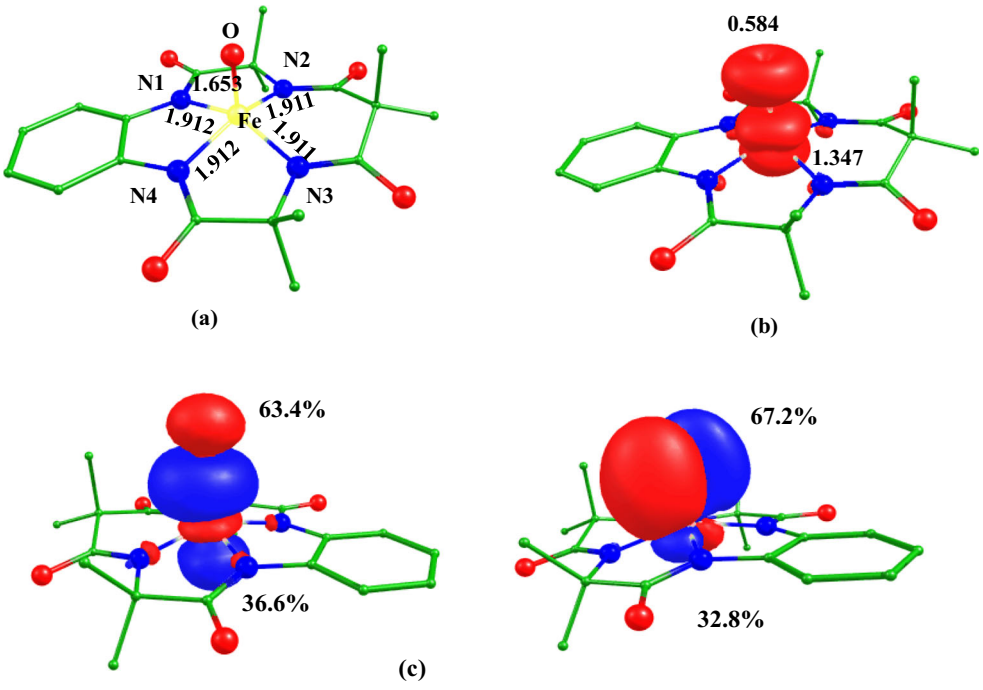

Fig. 8 **a** B3LYP-D2-optimized structure (bond length in Å) of $^3V_{is}$, **b** its spin density plot, and **c** computed NBO plots of $^3V_{is}$

of ESI). The Fe–O bond length is found to be 1.653 Å, shorter than that of the other spin surface quintet and singlet states (see Table S1 of ESI), and this shorter bond length is due to the formation of π bond between iron and oxygen revealing a double-bond character (see Scheme S2 of ESI). The Fe–O bond length matches with previous experimental and theoretical studies [53].

The orbital contribution of iron d_z^2 (36.6%) and oxygen p_z (63.4%) suggests the formation of the σ-bond (see Fig. 8c). However, additional orbital contributions between iron and oxygen atoms show the formation of the π-bond and unfold the presence of a double-bond character between them. The electronic configuration of the ground state is computed to be $(d_{xy})^2$, $(d_{yz})^1$, $(d_{xz,})^1$, $(d_z^2)^0$, and $(d_x^2{}_{-y}^2)^0$ (see Fig. 9), also supporting the formation of the π-bond between d_{yz} and p-orbital of the oxygen (see Fig. 8c). A similar electronic configuration is also found with other iron(IV)-oxo species [53]. Here, the $d_x^2{}_{-y}^2$ orbital has higher energy than the d_z^2 due to the strong equatorial ligand field of the TAML ligand. The stretching frequency of the Fe–O bond is found to be 880 cm^{-1} revealing the strength of the bond. The computed $Fe–N_{avg}$ bond length is found to be 1.971 Å, and this is longer than that of species I. The iron center of this species is also shifted towards the z-axis by 0.35 Å (see Table S3 of ESI). The computed HOMO-LUMO gap is 3.605 eV (see Fig. 10a). The computed spin density value of 1.347 is located at the iron center and the ferryl oxygen has also acquired spin density ($\rho = 0.584$). The coordinated nitrogen atoms also gained some spin density via electron delocalization. A significant spin density at the oxygen atom can activate the C–H/O–H bond of aliphatic/aromatic hydrocarbons [71–74].

Electronic structure and spin energetics of [(TAML)Fe^{V}–O]$^{-}$ species (VI)

One electron oxidation of species V can produce the [(TAML)Fe^{V}–O]$^{-}$ (species VI), and this species with sufficient thermal stability for extensive spectroscopic characterization was generated by de Oliveira et al. [50]. In our previous study, we have found that the low spin state ($S = 1/2$) of species VI is the ground state with the high spin lying at 5.2 kJ/mol higher in energy [99]. The computed Fe–O bond length is found to be smaller than that of species V (see Table S1 of ESI), and this is due to the increment in the double-bond character between the iron center and oxygen atom. The computed HOMO-LUMO gap is 1.423 eV, smaller than that of species V (see Fig. 10). The shift in the position of the iron atom is computed to be 0.40 Å. The redox potential change upon the oxidation at the iron center can also increase the reactivity of species (VI) [71, 100]. From the NBO calculations, we see that iron d_z^2 (39.2%) which is greater than species VI and oxygen p_z (60.8%) suggests a stronger bond

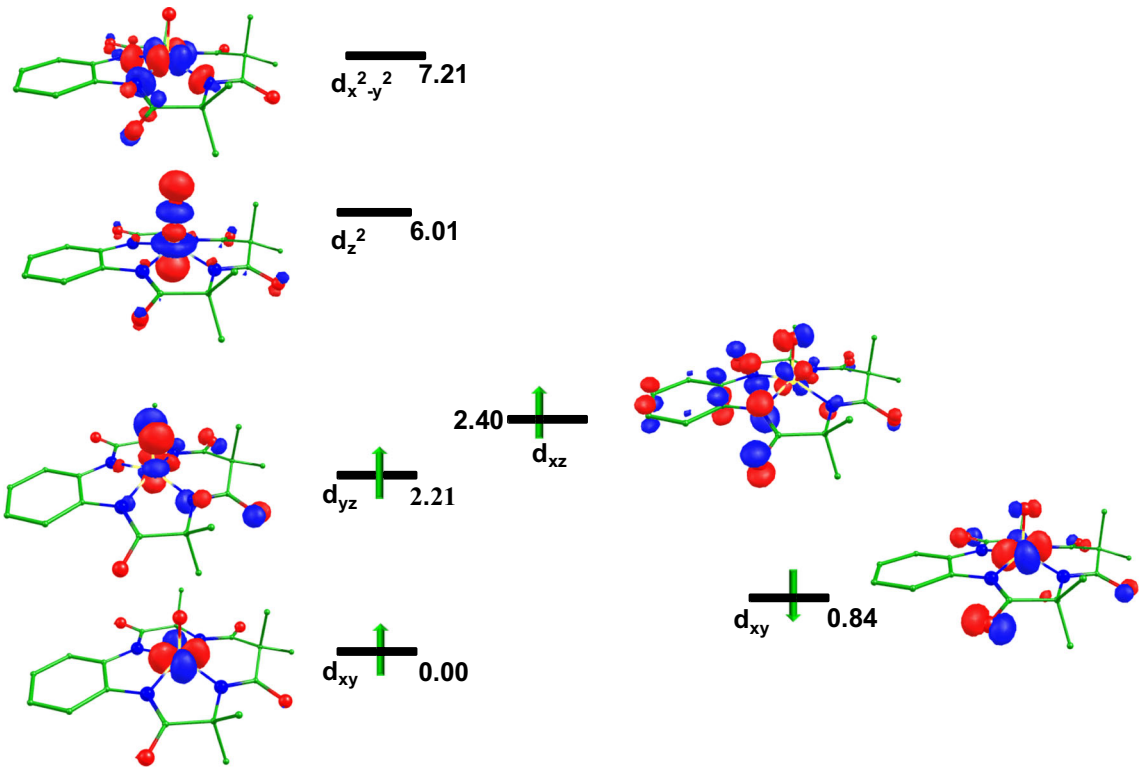

Fig. 9 Computed eigenvalue plot incorporating energies computed for d-based orbitals for alpha and beta spin corresponding to the ground state ($^5V_{is}$) (energies are given in eV)

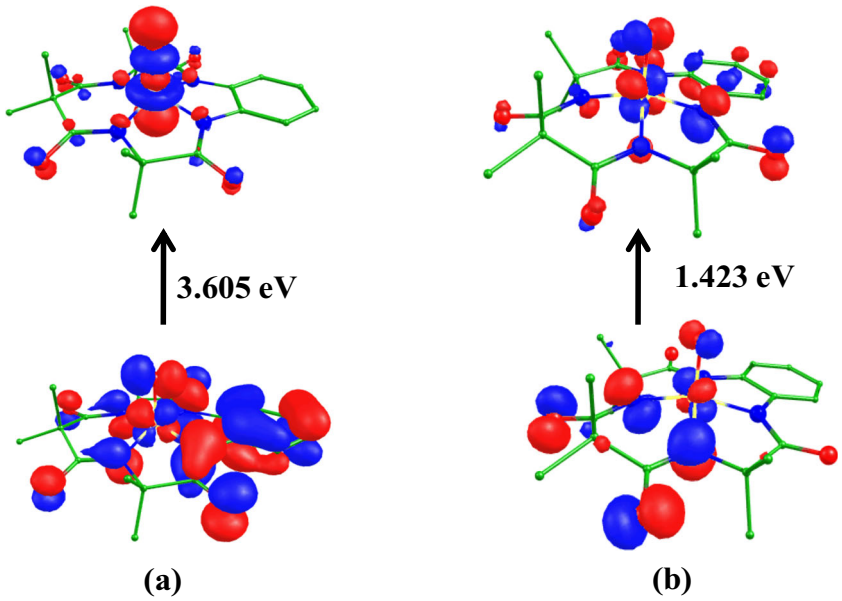

Fig. 10 The HOMO-LUMO frontier molecular orbitals of **a** species V and **b** species VI

between iron and oxygen than species V (see Fig. 8c and S8 of ESI). A spin density at the oxygen atom can help in C–H/O–H bond activation as well as in olefin epoxidation/sulfoxidation [50, 101].

Electronic structure and energetics of [(TAML)Fe^{IV}–μO–(TAML)Fe^{IV}]$^{2-}$ (species VII)

The well-characterized [(TAML)Fe^{V}–O]$^{-}$ species can react with Fe^{III}(TAML)] species I to generate μ-oxo dinuclear derivative [(TAML)Fe^{IV}–μO–Fe^{IV}(TAML)]$^{2-}$ (species VII) [50, 53]. This μ-oxo-bridged dinuclear species is also well characterized in previous studies [55]. The dimer [(TAML)Fe^{IV}–μO–Fe^{IV}(TAML)] (species VII) possesses the same ligand, and one can assume that both the iron centers are likely to have an identical spin on both the iron centers. There are five possible spin states such as $^{9}VII_{hs}$, $^{1}VII_{hs}$, $^{5}VII_{is}$, $^{1}VII_{is}$, and $^{1}VII_{ls}$ for species VII, and the schematically electronic interactions for each of the iron centers are shown in Table 1. We have optimized all five spin surfaces of species VII, and our DFT calculations predicted that the intermediate spin state ($^{1}VII_{is}$) with antiferromagnetic coupling between both the iron centers is found to be the ground state and other spin surfaces such as $^{9}VII_{hs}$, $^{1}VII_{hs}$, $^{5}VII_{is}$, and $^{1}VII_{ls}$ lie at 68.8, 82.4, 3.3, and 186.1 kJ/mol higher in energy, respectively. This ground state is also supported by experimental observation [55]. The optimized structure and spin density plot of the ground state ($^{1}VII_{is}$) and $^{5}VII_{is}$ are shown in Fig. 11. The Fe_1/Fe_2–N_{avg} bond lengths are found to be 1.913 Å and 1.895 Å which are greater than those of species I, and these are also in agreement with the experimental data [55]. The bond angle of Fe–O–Fe is found to be 160.5°, and this bending around the bridged oxygen atom is aroused due to the ligated nitrogen atom donating the electron density to the empty d_z^2 which overlaps to the *p*-orbital of the oxygen atom, and this also includes the double-bond formation between iron and oxygen atoms.

Our calculations also reveal that both the iron centers have equivalent formal charges, but there is a significant difference in Fe–O bond lengths. Computed Fe_1–μ-oxo and Fe_2–μ-oxo bond distances are found to be 1.835 Å and 1.711 Å, respectively, and these are also observed on similar structures in

Table 1 Possible spin states of [(TAML)Fe^{IV}–μO–Fe^{IV}(TAML)]$^{2-}$ species

	Electronic configuration		
Spin state	Fe(IV)	Fe(IV)	Relative energy(kJ/mol)
$^{9}VIII_{hs}$	$\pi^{*\uparrow}_{xz}\pi^{*\uparrow}_{yz}\delta^{\uparrow}_{xy}\sigma^{*\uparrow}_{z^2}\delta^{2}_{x^2-y^2}$	$\pi^{*\uparrow}_{xz}\pi^{*\uparrow}_{yz}\delta^{\uparrow}_{xy}\sigma^{*\uparrow}_{z^2}\delta^{2}_{x^2-y^2}$	68.8
$^{1}VIII_{hs}$	$\pi^{*\uparrow}_{xz}\pi^{*\uparrow}_{yz}\delta^{\uparrow}_{xy}\sigma^{*\uparrow}_{z^2}\delta^{2}_{x^2-y^2}$	$\pi^{*\downarrow}_{xz}\pi^{*\downarrow}_{yz}\delta^{\downarrow}_{xy}\sigma^{*\downarrow}_{z^2}\delta^{2}_{x^2-y^2}$	82.4
$^{5}VIII_{is}$	$\pi^{*\uparrow\downarrow}_{xz}\pi^{*\uparrow}_{yz}\delta^{\uparrow}_{xy}\sigma^{*\uparrow}_{z^2}\delta^{2}_{x^2-y^2}$	$\pi^{*\uparrow\downarrow}_{xz}\pi^{*\uparrow}_{yz}\delta^{\uparrow}_{xy}\sigma^{*\uparrow}_{z^2}\delta^{2}_{x^2-y^2}$	3.3
$^{1}VIII_{is}$	$\pi^{*\uparrow\downarrow}_{xz}\pi^{*\uparrow}_{yz}\delta^{\uparrow}_{xy}\sigma^{*\uparrow}_{z^2}\delta^{2}_{x^2-y^2}$	$\pi^{*\uparrow\downarrow}_{xz}\pi^{*\downarrow}_{yz}\delta^{\downarrow}_{xy}\sigma^{*\uparrow}_{z^2}\delta^{2}_{x^2-y^2}$	0
$^{1}VIII_{ls}$	$\pi^{*\uparrow\downarrow}_{xz}\pi^{*\uparrow\downarrow}_{yz}\delta_{xy}\sigma^{*\uparrow}_{z^2}\delta^{2}_{x^2-y^2}$	$\pi^{*\uparrow\downarrow}_{xz}\pi^{*\uparrow\downarrow}_{yz}\delta_{xy}\sigma^{*\uparrow}_{z^2}\delta^{2}_{x^2-y^2}$	186.1

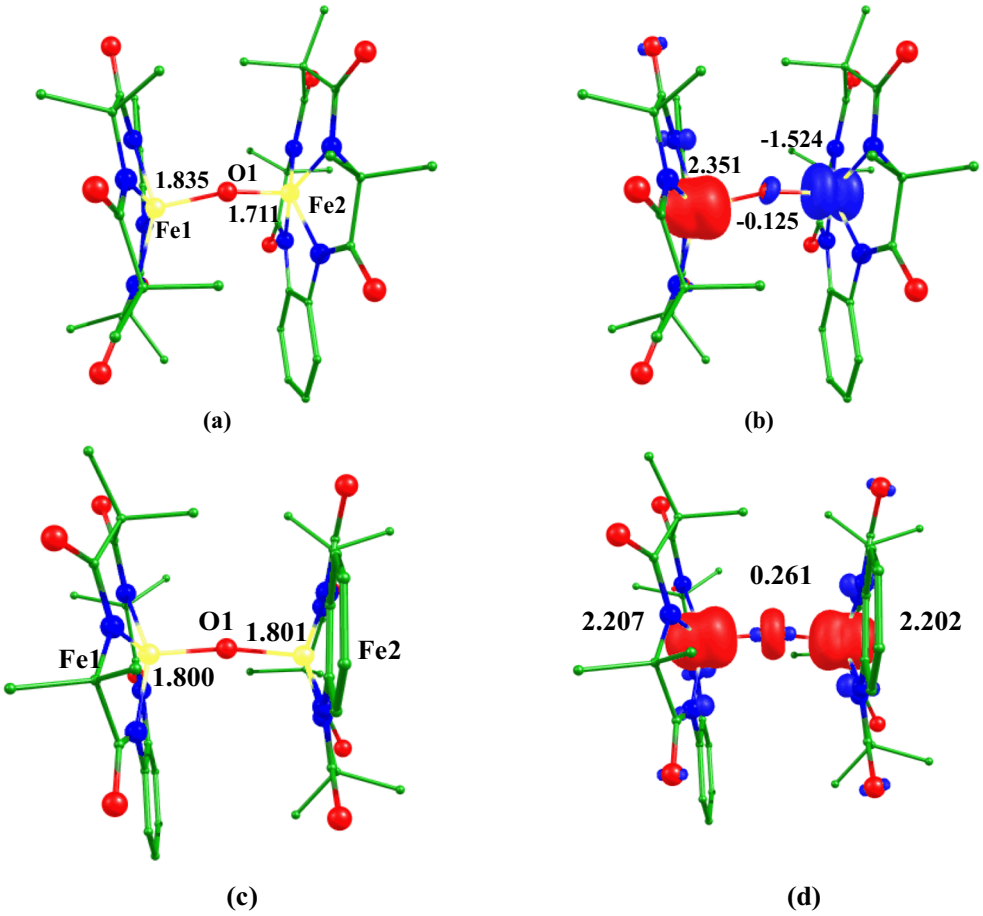

Fig. 11 **a** B3LYP-D2-optimized structure (bond length in Å) of $^{1}VII_{is}$ and its **b** spin density plot and **c** optimized structure (bond length in Å) of $^{5}VII_{is}$ and **d** its spin density plot

previous reports [73]. Selected bond length and spin density values are shown in Tables S1 and S2 of ESI.

The iron atom (Fe_2) possessing a beta electron (the negative spin density in Fig. 11b) has a shorter Fe–O bond length compared to the other Fe atom. From the NBO analysis, σ-bonding effects are also observed between the iron Fe_1 (19%) and μ-oxo (81%) whereas the Fe_2–μ-oxo possesses the additional π-bond character as the Fe_2 (25.9%) and μ-oxo (74.1%) orbital contribution is detected (see Fig. 12). Spin density on both the iron centers is found to be 2.351 and − 1.524, respectively. There is also a significant electron density found at the oxygen atom. From the earlier report, di-μ-oxo-diiron(VII) species and two μ-oxo groups yield a symmetric Fe(IV)-oxo environment [102]. Here, our calculations suggest an asymmetric environment with one shorter and other longer Fe–O bond lengths due to the presence of one μ-oxo group [73]. The Fe–Fe bond distance is 3.495 Å. From Table S4 of ESI, we see that the displacements along the *z*-axis are − 0.41 Å and 0.42 Å, and these opposite signs indicate that both iron centers

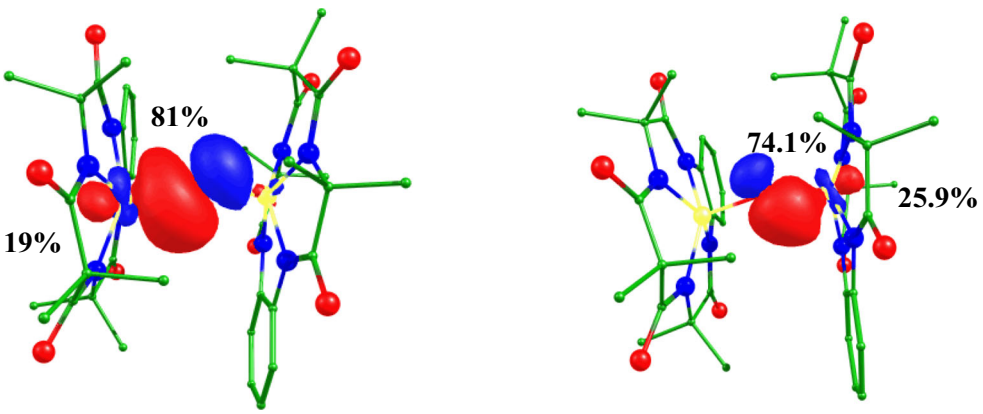

Fig. 12 Computed NBO plots of the ground state of species VII

are approaching towards each other. Nitrogen atoms coordinated to the iron atom gain significant electron density via the electron delocalization mechanism. The bridged oxygen atom possesses a significant electron density that can help in C–H/O–H bond activation [72, 73]. The eigenvalue plot is shown in Fig. 13, and both the Fe atoms have the similar electronic configuration of $(d_{xy})^2$, $(d_{yz})^1$, $(d_{xz})^1$, $(d_z^2)^0$, and $(d_{x^2-y^2})^0$ with alpha electrons in d_{xz} and d_{yz} at the Fe_1 center and beta electrons in d_{xz} and d_{yz} at the Fe_2 center (see Fig. 13). The d_z^2 and $d_{x^2-y^2}$ are unoccupied due to being much higher in energy. The HOMO-LUMO gap is 0.939 eV (see Fig. 14a).

The computed magnetic exchange coupling constant is found to be $J = -88.82\ cm^{-1}$, and this shows that antiferromagnetic coupling occurs between both the iron centers. The stretching frequencies for Fe_1–μO and Fe_2–μO are 349 cm^{-1} and 766 cm^{-1} respectively, and these frequencies are supported by the iron–μ-oxo bond distances.

Electronic structure and spin energetics of [(TAML)Fe^{IV}–O–O–Fe^{IV}(TAML)]$^{2-}$ (species VIII)

When they react in 1:2 of species I and dioxygen, oxygen-bridged dinuclear (μ–1,2-peroxo) species ([(TAML)Fe^{IV}–O–O–Fe^{IV}(TAML)]$^{2-}$ (species VIII) can be generated [55]. Similar to species VII, we have also optimized five possible spin states (see Table S6 of ESI) and our DFT calculations

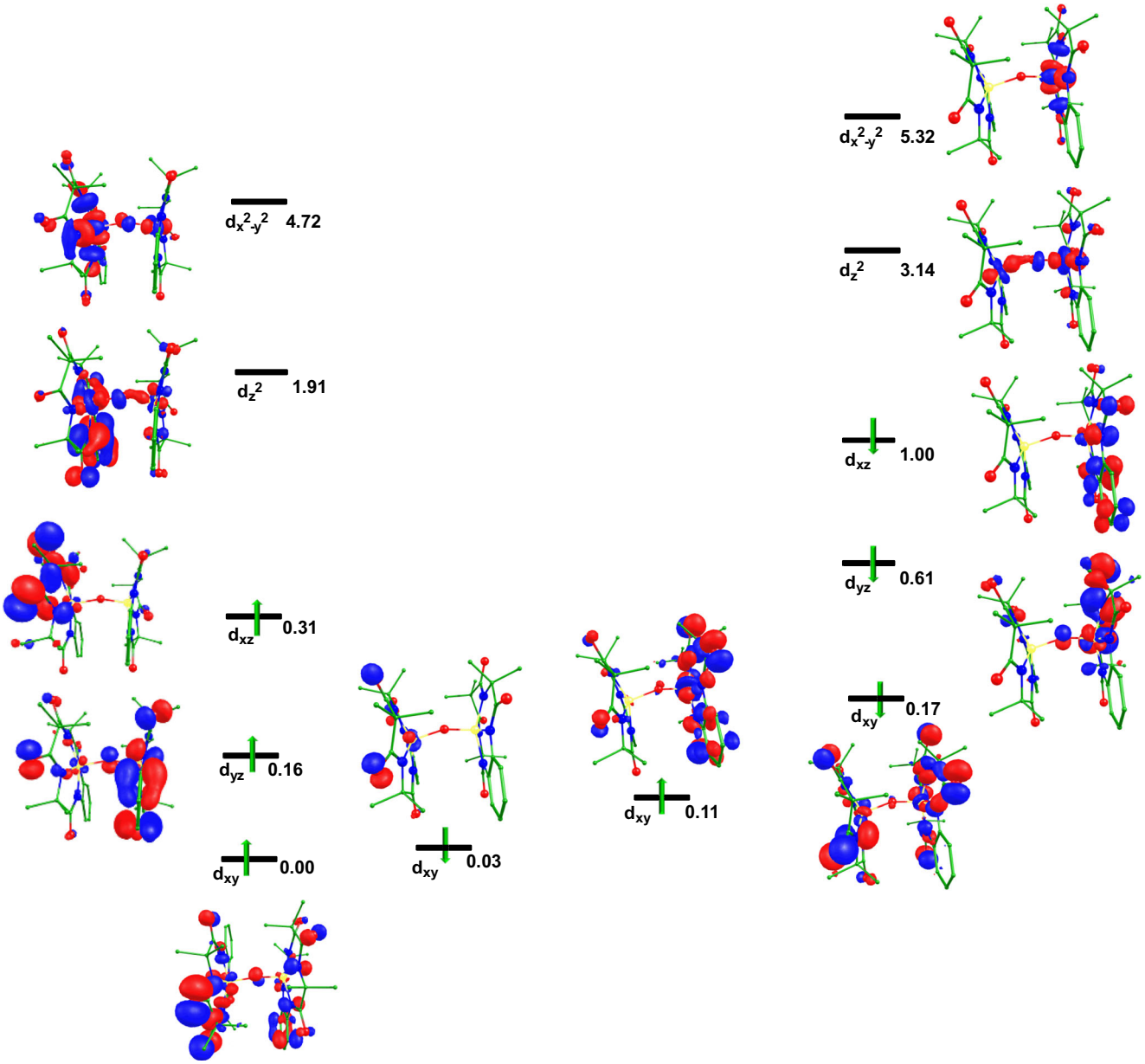

Fig. 13 Computed eigenvalue plot incorporating energies computed for *d*-based orbitals for alpha and beta spin corresponding to the ground state ($^1VII_{is}$) (energies are given in eV)

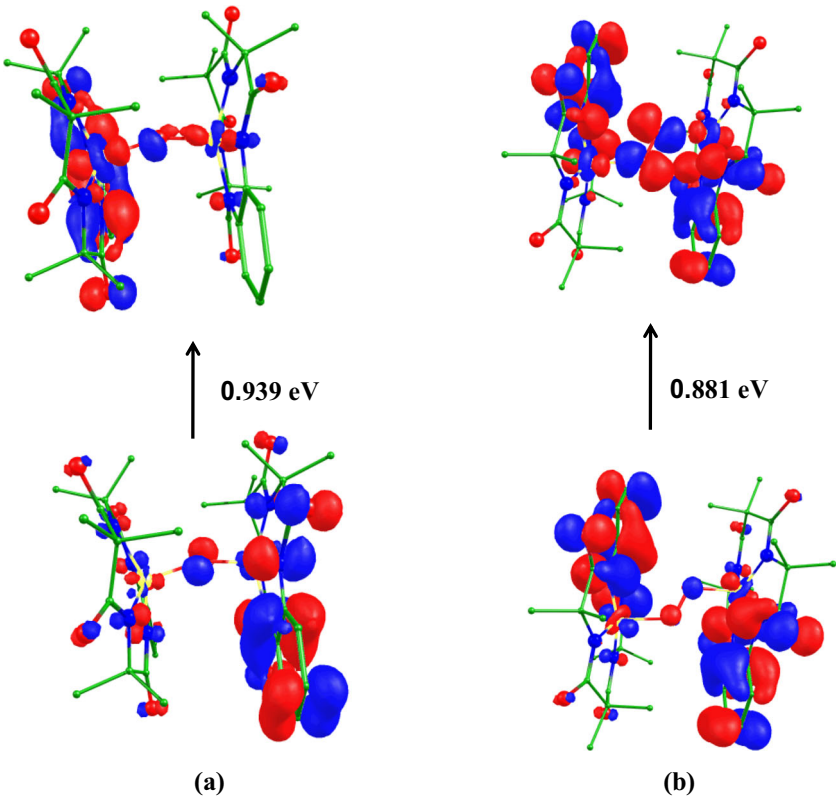

Fig. 14 The HOMO-LUMO frontier molecular orbitals of species VII ($^{1}VII_{is}$) and species VIII ($^{5}VIII_{is}$)

show that the $^{5}VIII_{is}$ is found to be the ground state with $^{9}VIII_{hs}$, $^{1}VIII_{is}$, and $^{1}VIII_{ls}$ lying at 36.2, 13.0, 12.9, and 356.3 kJ/mol higher in energy, respectively. The optimized structure and spin density plot of the $^{5}VIII_{is}$ (ground state) and the corresponding spin state ($^{1}VIII_{is}$) are shown in Fig. 15. The calculated Fe_1–μO1 and Fe_2–μO2 bond lengths of the $^{5}VIII_{is}$ state are found to be 2.124 Å and 2.127 Å, respectively, and are higher than the corresponding bond lengths of species $^{1}VII_{is}$. The O_1–O_2 bond length is 1.334 Å, in agreement with that of the other –1,2-peroxo species [103], and the computed stretching frequency for the O–O bond is ν1050 cm^{-1} corresponding to the formation of the peroxo linkage. The same stretching frequencies (ν258 cm^{-1}) are found for both Fe_1–O_1 and Fe_2–O_2 bonds, smaller than those of the μ-oxo-bridged species, indicating that the Fe–O bond length is longer in μ–1,2-peroxo species and suggesting the presence of a single bond between both the iron–oxygen bonds (see Table S1 of ESI). The Fe_1–N_{avg} and Fe_2–N_{avg} bond distances are computed to be 1.882 Å and 1.883 Å, respectively. The spin density plot of the ground state shows that

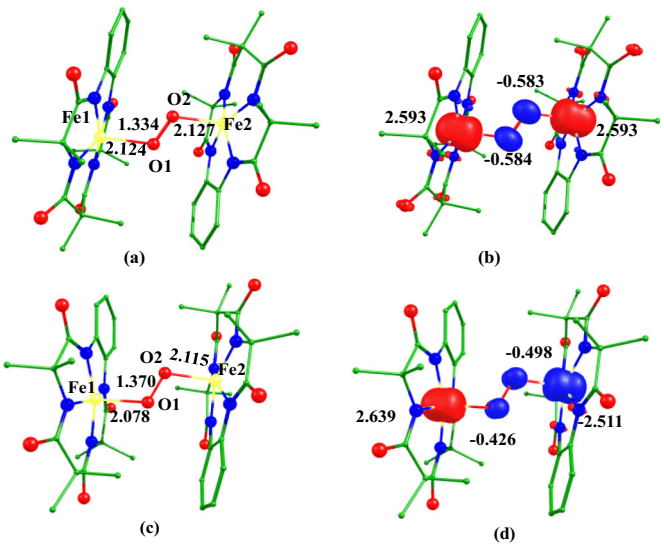

Fig. 15 **a** B3LYP-D2-optimized structure (bond length in Å) of $^{5}VIII_{is}$ and **b** its spin density plot and **c** optimized structure (bond length in Å) of $^{1}VIII_{is}$ and **d** its spin density plot

both the iron centers possess the same sign of spin density suggesting the presence of ferromagnetic coupling between iron centers, and this is also supported by the estimation of the magnetic exchange with the value of 777.44 cm^{-1}, although the experimental magnetic exchange value of the species is not observed yet. The coordinated nitrogen atoms to the iron center also acquired electron density due to electron delocalization. The computed HOMO-LUMO gap is smaller than that of species VII (see Fig. 14b). Similar to species VII, here also, displacements along the *z*-axis have an opposite sign 0.04 Å and -0.07 Å— indicating that both iron centers are approaching towards each other, this displacement is smaller as compared to that of species VII. The eigenvalue plot also describes the electronic configurations around both the iron centers (see Fig. 16). It is also found that orbitals of both the Fe atoms are found to be at the same energy levels, and the electronic configuration is found to be $(d_{xy})^2$, $(d_{yz})^1$, $(d_{xz,})^1$, $(d_z^2)^0$, and $(d_{x^2-y^2})^0$. The d_z^2 and $d_{x^2-y^2}$ are unoccupied due to being much higher in energy. The cleavage of the peroxo linkage can generate $[(TAML)Fe^{IV}–O]^{2-}$ species V and $[(TAML)Fe^{V}–O]^{-}$ species VI. Significant electron densities are also located at both the bridged oxygen atoms which can activate C–H and O–H bonds of aliphatic and aromatic compounds [71, 73, 98]. The HOMO-LUMO gap is shown in Fig. 14b, and the gap in species VII is smaller than that in species VIII. NBO analysis shows 6.7% of Fe_1–p_y and 93.3% of O–p_x and 6.7% of Fe_2-p_y and 93.3% of O-p_x (see Fig. S9 of ESI). The contribution of the iron orbital is small as compared

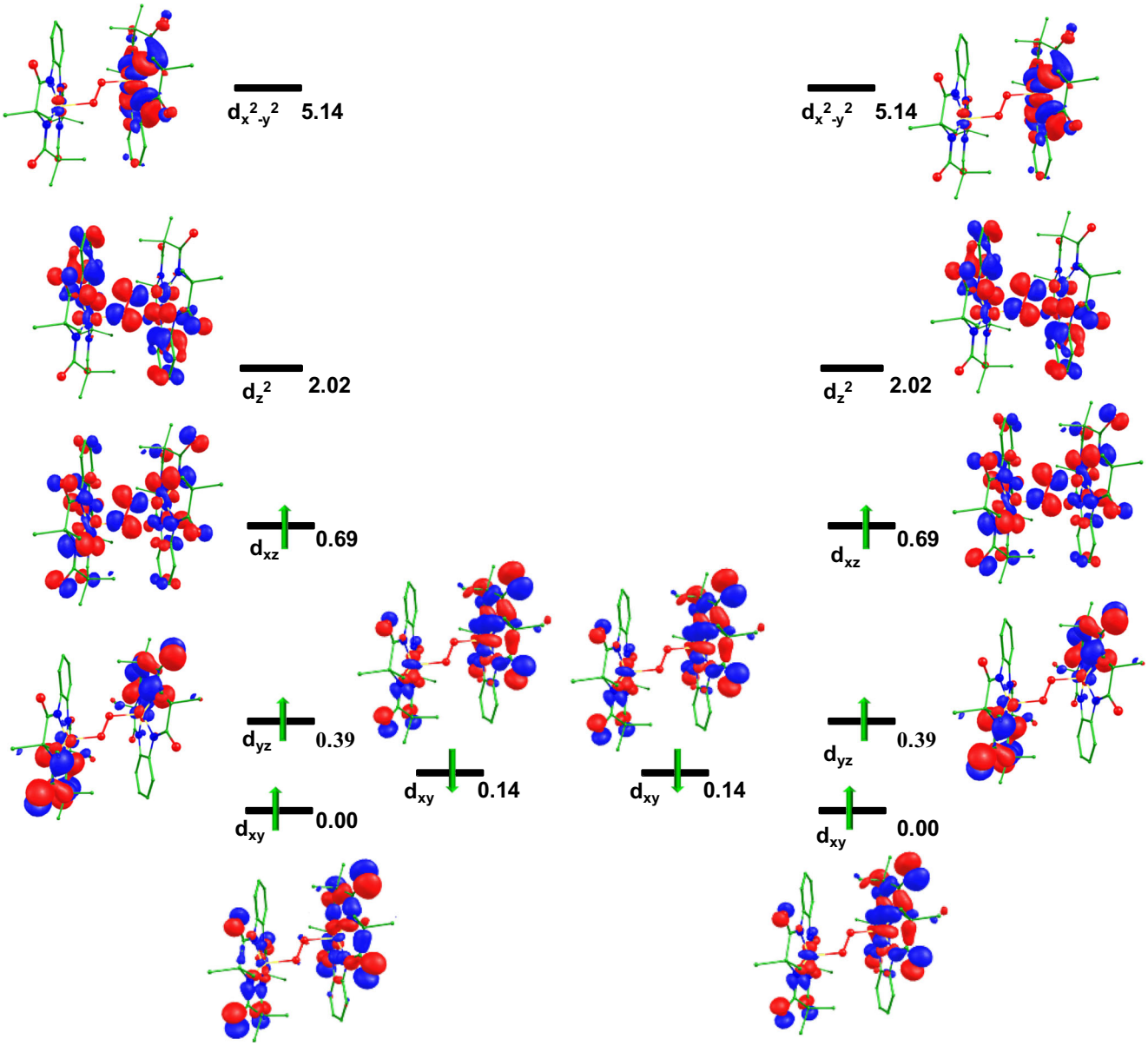

Fig. 16 Computed eigenvalue plot incorporating energies computed for *d*-based orbitals for alpha and beta spin corresponding to the ground state ($^5VIII_{is}$) (energies are given in eV)

to that of the μ-oxo-bridged complex iron atom, and this may be due to the longer bond length and also the absence of the π-bond between $Fe_{1/2}$ and $\mu O_{1/2}$ as compared to Fe_1–O_1 and Fe_2-O_1 of μ-oxo-bridged species.

Comparative study

Species formed after the reactions depend upon the binding modes of dioxygen either η^1 (end-on species) or η^2 (side-on species). Here, species I–VI are mononuclear whereas species VII–VIII are bridged dinuclear. Our computed parameters also show that the Fe_1–O_1 bond distance of species II (2.173 Å) is longer than that of species III (1.994 Å), whereas the O_1–O_2 bond length of species II (1.321 Å) is smaller than that of species III (1.537 Å) due to both the oxygen atoms coordinated to the iron center in species III, and these are also supported by computed stretching frequencies. The shifting of the iron center of species II (0.08 Å) out of the plane is found to be smaller than that of species III (0.72 Å), due to repulsion between charges of the coordinated atoms of both the oxygen atoms that forces the iron atom out of the plane which is comparatively more in species III. The HOMO-LUMO gap of species II (1.524 eV) is computed to be smaller than that of species III (3.698 eV). The Fe–O_1 bond distance of species IV (1.889 Å) is smaller than that of species II (2.173 Å) and species III (1.994 Å) which may be due to being protonated at the distal oxygen atom (–OOH). The HOMO-LUMO gap in species IV (0.059 eV) is smaller than that in species II and species III. The shift of the iron atom out of the plane in species V (0.19 Å) is larger than that in species II (0.08 Å) but smaller than that in species III (0.72 eV).

In species V, the Fe–N_{avg} (1.911 Å) and Fe–O (1.653 Å) bond lengths are longer than those in species VI (1.892 Å and 1.630 Å for Fe–N_{avg} and Fe–O). The shift of the iron atom out of the plane in species VI (0.40 Å) is calculated to be larger than that in species V (0.35 Å), and this may be due to the reflection of higher charge at the iron center. The HOMO-LUMO gap of species V (3.605 eV) is larger than that of species VI (1.423 eV) indicating higher reactivity of species VI which is also observed in previous reports [53, 71, 104, 105]. From the NBO analysis of species V and species VI, we have observed that both species V and species VI have a double-bond character, In species VI, the iron atom has 39.2% contribution which is slightly greater than that in species V (36.6%) which indicates that the Fe–O bond has a more double-bond character in species VI than in species V.

In dinuclear species VII and VIII, the Fe_1/Fe_2–N_{avg} computed bond distances (1.913 Å and 1.895 Å, respectively) are longer than the corresponding bond (1.882 Å and 1.883 Å, respectively) in species VIII, but iron–μ-oxo bond lengths (1.835 Å and 1.777 Å, respectively) of species VII are longer than iron–oxygen bonds (2.124 Å and 2.127 Å, respectively) of species VIII, and these are also supported by the computed stretching frequencies. From the NBO analysis of species VII, we have found that orbital contribution of 19% at the Fe_1 center and 25.9% at the Fe_2 center indicates that Fe_2–O_1 has a double-bond contribution which is also supported by the smaller bond Fe_2–O_1 bond distance. NBO analysis for species VIII has a small contribution at iron centers (6.7%) supporting the longer Fe_1–O_1 and Fe_2–O_2 bond lengths. The shift of the iron atom out of plane along the bridged oxygen (axial ligand) of species VII (− 0.41 Å/0.42 Å for Fe_1/Fe_2) is longer than that of species VIII (0.04 Å/− 0.07 Å for Fe_1/Fe_2). The HOMO-LUMO gap of species VII (0.939 eV) is larger than that of species VIII (0.881 eV). Both the iron centers in species VII are antiferromagnetically coupled, while in species VIII, both iron centers are ferromagnetically coupled. The HOMO-LUMO gap in binuclear species is relatively smaller than that in mononuclear species except for species IV.

Conclusions

Tetraamido macrocyclic ligand-coordinated iron species are of great interest because of their wide role in catalytic reactions, and they mimic properties of metalloenzymes. Here, we have undertaken the DFT study on mononuclear and dinuclear iron–TAML species for analyzing structures, bonding, energetics, and magnetic interactions. Some salient conclusions derived from this work are highlighted below:

(i) Our computed DFT energies using dispersion-corrected hybrid B3LYP-D2 functional predicted the intermediate spin state for $[Fe^{III}(TAML)]^-$ (species I), $[(TAML)Fe^{IV}–\eta^1–O_2]^{\bullet-}$ (species II), $[(TAML)Fe^{IV}–OOH]^-$ (species IV), $[(TAML)Fe^{IV}–O]^{2-}$ (species V), $[(TAML)Fe^{IV}–\mu O–(TAML)Fe^{IV}]^{2-}$ (species VII), and $[(TAML)Fe^{IV}–\mu O_2–Fe^{IV}(TAML)]^{2-}$ (species VIII); the high spin state for $[(TAML)Fe^{III}–\eta^1–O_2]^{3-}$ (species IIIa) and the low spin state for $[(TAML)Fe^{V}–O]^-$ species (VI) are computed as the ground state. These ground states are in good agreement with the available experimental species [39, 53, 55, 56].

(ii) Our computed DFT results also show that antiferromagnetic coupling between both iron centers is found to be in μ-oxo-bridged species VII whereas ferromagnetically coupling is in μ–(1,2-peroxo) species VIII.

(iii) Here, we have also observed that the computed Fe–N_{avg} bond length of species I is smaller than that of the rest of the studied species (species II–VIII).

(iv) The increase in the oxidation state increases the bond strength confirmed by decreases in the bond length and an increase in stretching frequency.

(v) The iron atom gets out of the plane on reaction with dioxygen, the shift of the position of the iron atom along

the z-axis of the mononuclear species is computed to be 0.08 Å (species II), 0.72 Å (species III), 0.19 Å (species IV), 0.35 Å (species V), and 0.40 Å (species VI), and the shift of the position of the iron atom along the z-axis of the dinuclear species is computed to be − 0.41 Å/0.42 Å for Fe_1/Fe_2 (species VII) and 0.04 Å/− 0.07 Å for Fe_1/Fe_2 (species VIII).

(vi) NBO analysis, orbital contributions of iron and oxygen, and iron atoms explained the ionic and the covalent nature of a metal–oxygen bond along with the formation of the π-bond.

(vii) The nitrogen atom coordinated to the iron atom gains electron density via the electron delocalization mechanism. The significant spin density at the oxygen atom can be a witness for C–H/O–H/N–H bond activation.

To this end, these findings have direct relevance to the community working in the area of iron complexes/bioinorganic chemistry and related interface of chemistry.

Supplementary Information The online version contains supplementary material available at https://doi.org/10.1007/s11224-020-01690-x.

Acknowledgments AA would like to thank the Central University of Haryana, Mahendergarh, for providing infrastructure and also Prof. G. Rajaraman for computational help.

Author contribution Monika is responsible for the conceptualization analysis and wrote the results and discussion. Oval Yadav wrote the introduction and edited the manuscript. Hemlata Chauhan is responsible for the methodology and structures. Azaj Ansari supervised the study.

Funding information AA would like to acknowledge the financial support received from the Government of India through the SERB-DST (ECR/2016/001111). Monika would like to thank UGC New Delhi for the SRF fellowship, and OY thanks CSIR New Delhi for the SRF fellowship.

Data availability Now we have given XYZ coordinates of optimized structures in the Supplementary Material.

Compliance with ethical standards

Conflict of interest The authors declare that they have no conflict of interest.

Consent to publish All authors provided consent to publish.

References

1. Nam W (2015). Acc Chem Res 8:2415
2. Barman P, Upadhyay P, Faponle AS, Kumar J, Nag SS, Kumar D, Sastri CV, de Visser SP (2016). Angew Chem Int Ed 55:11091
3. Jackson TA, Rohde J-U, Seo MS, Sastri CV, DeHont R, Stubna A, Ohta T, Kitagawa T, Munck E, Nam W, Que Jr L (2008). J Am Chem Soc 130:12394
4. Dhuri SN, Cho K-B, Lee YM, Shin SY, Kim JH, Mandal D, Shaik S, Nam W (2015). J Am Chem Soc 137:8623
5. Lee Y-M, Dhuri SN, Sawant SC, Cho J, Kubo M, Ogura T, Fukuzumi S, Nam W (2009). Angew Chem Int Ed 48:1803
6. Dhuri SN, Seo MS, Lee Y-M, Hirao H, Wang Y, Nam W, Shaik S (2008). Angew Chem Int Ed 47:3356
7. Dhuri SN, Lee Y-M, Seo MS, Cho J, Narulkar DD, Fukuzumi S, Nam W (2015). Dalton Trans 44:7634
8. Punniyamurthy T, Velusamy S, Iqbal J (2005). J Chem Rev 105:2329
9. Nam W (2007). Acc Chem Res 40:522
10. Shaik S, Lai W, Chen H, Wang Y (2010). Acc Chem Res 43:1154
11. de Montellano PRO (2010). Chem Rev 110:932
12. Wackett LP (2002). Enzym Microb Technol 31:577
13. Horn EJ, Rosen BR, Chen Y, Tang J, Chen K, Eastgate MD, Baran PS (2016). Nature 533:77
14. Nakamura A, Nakada M (2013). Synthesis 45:1421
15. Garcia-Cabeza AL, Moreno-Dorado FJ, Ortega MJ, Guerra FM (2016). Synthesis 48:2323
16. White MC (2012). Synlett 23:2746
17. Jazzar R, Hitce J, Renaudat A, Sofack-reutzer J, Baudoin O (2010). Chem Eur J 16:2654
18. Groves JT (2006). J Inorg Biochem 100:434
19. Groves JT, Haushalter RC, Nakamura M, Nemo TE, Evans BJ (1981). J Am Chem Soc 103:2884
20. Groves JT, Nemo TE (1983). J Am Chem Soc 105:6243
21. Meunier B (1992). Chem Rev 92:1411
22. Costas M, Mehn MP, Jensen MP, Que Jr L (2004). Chem Rev 104:939
23. Que Jr L (2007). Acc Chem Res 40:493
24. Hitomi Y, Arakawa K, Funabiki T, Kodera M (2012). Angew Chem 124:3504
25. Talsi EP, Bryliakov KP (2012). Coord Chem Rev 256:1418
26. Zhang Q, Gorden JD, Goldsmith CR (2013). Inorg Chem 52:13546
27. Lindhorst AC, Haslinger S, Kuhn FE (2015). Chem Commun 51:17193
28. Oloo WN, Que Jr L (2015). Acc Chem Res 48:2612
29. Sankaralingam M, Lee Y-M, Nam W, Fukuzumi S (2017). Inorg Chem 56:5096
30. Cavani F, Teles JH (2009). Chem Sus Chem 2:508
31. Osterberg PM, Niemeier JK, Welch CJ, Hawkins JM, Martinelli JR, Johnson TE, Root TW, Stahl SS (2015). Org Process Res Dev 19:1537
32. Backvall J-E (2004) Modern oxidation methods. Weinheim, Wiley-VCH Verlag GmbH
33. Solomon EI, Wong SD, Liu LV, Decker A, Chow MS (2009). Curr Opin Chem Biol 13:99
34. Abu-Omar MM, Loaiza A, Hontzeas N (2005). Chem Rev 105:2227
35. Solomon EI, Neidig ML (2005). Chem Commun 105:2227
36. Chen MS, White MC (2007). Science 318:783
37. Chen MS, White MC (2010). Science 327:566
38. Gormisky PE, White MC (2013). J Am Chem Soc 135:14052
39. Chanda A, Popescu D-L, de Oliveira FT, Bominaar EL, Ryabov AD, Munck E, Collins TJ (2006). J Inorg Biochem 100:606
40. Sahu S, Goldberg DP (2016). J Am Chem Soc 138:11410
41. Kovaleva EG, Lipscomb JD (2008). Nat Chem 4:186
42. Pau MYM, Lipscomb JD, Solomon EI (2007). Proc Natl Acad Sci U S A 104:18355
43. Jasniewski AJ, Que Jr L (2018). Chem Rev 118:2554
44. Huang X, Groves JT (2018). Chem Rev 118:2491
45. Solomon EI, Goudarzi S, Sutherlin KD (2016). Biochemistry 55:6363
46. Wang J, Sun H, Zhao XS (2010). Catal Today 158:263
47. Institute for Green Oxidation Chemistry, unpublished results

48. Collins TJ (2002). Acc Chem Res 35:782
49. Chanda A, de Oliveira FT, Collins TJ, Munck E, Bominaar EL (2008). Inorg Chem 47:9373
50. de Oliveira FT, Chanda A, Banerjee D, Shan X, Mondal S, Que Jr L, Bominaar EL, Münck E, Collins TJ (2007). Science 315:835
51. Collins TJ, Walter C (2006) Little green molecules. Sci Am 294: 82
52. Collins TJ, Gordon-Wylie SW, Bartos MJ, Horwitz CP, Woomer CG, Williams SA, Patterson RE, Vuocolo LD, Paterno SA, Strazisar SA, Peraino DK, Dudash CA (1998) In: Anastas PT, Williamson TC (eds) Green chemistry: environmentally benign chemical syntheses and processes. Oxford University Press, Oxford, pp 46–71
53. Pattanayak S, Jasniewski JA, Rana A, Draksharapu A, Singh KK, Weitz A, Hendrich M, Que Jr L, Dey A, Gupta SS (2017). Inorg Chem 56:6352
54. Nam W (2015). Acc Chem Res 48:2415
55. Ghosh A, de Oliveira FT, Yano T, Nishioka T, Beach ES, Kinoshita I, Munck E, Ryabov AD, Horwitz CP, Collins TJ (2005). J Am Chem Soc 127:2505
56. Hong S, Sutherlin KD, Park J, Kwon E, Siegler MA, Solomon EI, Nam W (2014). Nat Commun 5:5440
57. Fan R, Serrano-Plana J, Oloo WN, Draksharapu A, Delgado-Pinar E, Company A, MartinDiaconescu V, Borrell M, Lloret-Fillol J, Garcia-Espana E, Guo Y, Bominaar E, Que Jr L, Costas M, Munck E (2018). J Am Chem Soc 140:3916
58. Ghosh M, Pattanayak S, Dhar BB, Singh KK, Panda C, Gupta SS (2017). Inorg Chem 52:10852
59. Zou G, Jing D, Zhong W, Zhao F, Mao L, Xu Q, Xiao J, Yin D (2016). RSC Adv 6:3729
60. Boudjema S, Vispe E, Choukchou-Braham A, Mayoral JA, Bachir R, Fraile JM (2015). RSC Adv 5:6853
61. Ray K, Pfaff F, Wang B, Nam W (2014). J Am Chem Soc 136: 13942
62. Cho J, Sarangi R, Nam W (2012). Acc Chem Res 45:1321
63. Kang H, Cho J, Cho K-B, Nomura T, Ogura T, Nam W (2013). Chem Eur J 19:14119
64. Cho J, Kang HY, Liu LV, Sarangi R, Solomon EI, Nam W (2013). Chem Sci 4:1502
65. Rohde J-U, In J-H, Lim MH, Brennessel WW, Bukowski MR, Stubna A, Munck E, Nam W, Que Jr L (2003). Science 299:1037
66. Seo MS, Kim NH, Cho K-B, So JE, Park SK, Clemancey M, Garcia-Serres R, Latour J-M, Shaik S, Nam W (2011). Chem Sci 2:1039
67. Rohde J-U, Stubna A, Bominaar EL, Münck E, Nam W, Que Jr L (2006). Inorg Chem 45:6435
68. Pandey B, Jaccob M, Rajaraman G (2017). Chem Commun 53: 3193
69. Bell SR, Groves JT (2009). J Am Chem Soc 131:9640
70. Fukuzumi S, Morimoto Y, Kotani H, Naumov P, Lee Y-M, Nam W (2010). Nat Chem 2:756
71. Ansari A, Kaushik A, Rajaraman G (2013). J Am Chem Soc 135: 4235
72. Ansari M, Vyas N, Ansari A, Rajaraman G (2015). Dalton Trans 44:15232
73. Ansari A, Ansari M, Singha A, Rajaraman G (2017). Chem Eur J 23:10110
74. Kumar R, Ansari A, Rajaraman G (2018). Chem Eur J 24:6660
75. Yachandra V, Sauer K, Klein M (1996). Chem Rev 96:2927
76. Karlsson A, Parales J, Parales R, Gibson D, Eklund H, Ramaswamy S (2003). Science 299:1039
77. Frisch MJ, Trucks GW, Schlegel HB, Scuseria GE, Robb MA, Cheeseman JR, Scalmani G, Barone V, Ennucci B, Petersson GA, Nakatsuji H, Caricato M, Li X, Hratchian HP, Izmaylov AF, Bloino J, Zheng G, Sonnenberg JL, Hada M, Ehara M, Toyota K, Fukuda R, Hasegawa J, Ishida M, Nakajima T, Honda Y, Kitao O, Nakai H, Vreven T, Montgomery Jr JA, Peralta JE, Ogliaro F, Bearpark M, Heyd JJ, Brothers E, Kudin KN, Staroverov VN, Keith T, Kobayashi R, Normand J, Raghavachari K, Rendell A, Burant JC, Iyengar SS, Tomasi J, Cossi M, Rega N, Millam JM, Klene M, Knox JE, Cross JB, Bakken V, Adamo C, Jaramillo J, Gomperts R, Startmann RE, Yazyev O, Austin AJ, Cammi R, Pomelli C, Ochterski JW, Martin RL, Morokuma K, Zakrzewski VG, Voth GA, Salvador P, Dannenbergy JJ, Dapprich S, Daniels AD, Farkas O, Foresman JB, Ortiz JV, Cioslowski J, Fox DJ (2009) GAUSSIAN 09 Revision(A.01). Gaussian, Inc, Wallingford
78. Grimme SJ (2006). Comput Chem 27:1787
79. Dunning Jr TH, Hay PJ (1976) Modern theoretical chemistry (Ed: Schaefer, H), vol 3. Plenum, New York
80. Hay PJ, Wadt WR (1985). J Chem Phys 82:270
81. Hay PJ, Wadt WR (1985). J Chem Phys 82:299
82. Wadt WR, Hay PJ (1985). J Chem Phys 82:284
83. Schaefer A, Horn H, Ahlrichs R (1992). J Chem Phys 97:2571
84. Schaefer C, Huber C, Ahlrichs R (1994). Chem Phys 100:5829
85. Jomroz MH (2004) Vibrational energy distribution analysis, VEDA4, Warsaw
86. James C, Raj AA, Reghunathan R, Jayakumar VS, Joe IH (2006). J Raman Spectrosc 37:1381
87. Liu J, Chen Z, Yuan S (2005). J Zhejiang Univ Sci B 6:584
88. Noodleman L (1981). J Chem Phys 74:5737
89. Noodleman L, Davidson ER (1986). Chem Phys 109:131
90. Vaska L (1976). Acc Chem Res 9(175):80
91. Dickman MH, Pope MT (1994). Chem Rev 94:569
92. Shan X, Que Jr L (2005). Proc Natl Acad Sci USA 102:5340
93. Momenteau M, Reed CA (1994). Chem Rev 94:659
94. Kundu S, Matito E, Walleck S, Pfaff FF, Heims F, Babay R, Luis JM, Company A, Braun B, Glaser T, Ray K (2012). Chem Eur J 18:2787
95. Cramer CJ, Tolman WB, Theopold KH, Rheingold AL (2003). Proc Natl Acad Sci U S A 100:3635
96. Ansari A, Jayapal P, Rajaraman G (2015). Angew Chem Int Ed 127:564
97. Seo MS, Kim JY, Annaraj J, Kim Y, Lee Y-M, Kim SJ, Kim J, Nam W (2007). Angew Chem Int Ed 46:377
98. Grapperhaus CA, Mienert B, Bill E, Weyhermüller T, Wieghardt K (2000). Inorg Chem 39:5306
99. Monika, Ansari A (2020). New J Chem https://doi.org/10.1039/D0NJ03095C
100. Ansari A, Rajaraman G (2014). Phys Chem Chem Phys 16:14601
101. Kundu S, Thompson JVK, Ryabov AD, Collins TJ (2011). J Am Chem Soc 133:18546
102. Stoian S, Xue GQ, Bominaar EL, Que Jr L, Munck EJ (2014). Am Chem Soc 136:1545
103. Fukuzumi S, Mandal S, Mase K, Ohkubo K, Park H, Benet-Buchholz J, Nam W, Llobet A (2012). J Am Chem Soc 134:9906
104. Makhlynets OV, Das P, Taktak P, Flook M, Mas-Ballesté R, Rybak-Akimova EV, Que Jr L (2009). Chem Eur J 15:13171
105. Makhlynets OV, Rybak-Akimova EV (2010). Chem Eur J 16: 13995

Publisher's note Springer Nature remains neutral with regard to jurisdictional claims in published maps and institutional affiliations.